Real-Time Molecular Scale Observation of Crystal Formation

Roy E. Schreiber, [1] Lothar Houben,[2] Sharon G. Wolf,[2] Gregory Leitus,[2] Zhong-Ling Lang,[3] Jorge J. Carbó, [3] Josep M. Poblet,[3] and Ronny Neumann[1]*

Abstract: How do molecules in solution form crystal nuclei, which then grow into large crystals? The classical mechanism of homogeneous crystal nucleation claims crystal nucleation by spontaneous random aggregation of species from liquid or solution, while a non-classical mechanism claims formation of an amorphous dense phase that reorders to form stable crystal nuclei. It has been an unanswered experimental challenge to observe the formation of crystal nuclei of 5-30 molecules. Using polyoxometalates the research shows formation of small crystal nuclei that are observable by cryogenic transmission electron microscopy. Both "classic" and "non-classic" nucleation processes were observed depending on the cation present. The experiment verifies theory showing that "non-classic" nucleation is lower in energy. The arrangement of even seven molecules fit the order found by X-ray diffraction of a single bulk crystal demonstrating that a proto-crystal of the same structure has been formed.

[1]Department of Organic Chemistry, Weizmann Institute of Science, Rehovot, Israel 76100.

[2]Department for Chemical Research Support, Weizmann Institute of Science, Rehovot, Israel 76100.

[3]Departament de Química Física i Inorgànica, Universitat Rovira i Virgili, Marcel·lí Domingo 1, 43007-Tarragona, Spain.

According to the classical mechanism of homogeneous crystal nucleation, a crystal nucleus is first formed by spontaneous random aggregation of species from liquid or solution[1,2]. This crystal nucleus can then grow by molecular attachment to form a full crystal. It has been noted that the initial aggregation of molecules is energetically unfavorable due to large surface tension[3,4]. Therefore, growing a thermodynamically stable crystal nucleus requires overcoming a high-energy barrier and the rapid random assembly of a few molecules. The high energy barrier can be bypassed by heterogeneous crystal nucleation where a foreign species serves as a base for molecular attachment, thereby overcoming the high surface tension of the newly formed crystal nucleus. In essence, this is catalysis of crystal nucleation[5-7]. However, in the absence of a heterogeneous seed, or in the case of negligible surface interaction, crystallization will also occur under homogeneous conditions[8-10]. More recently, evidence has arisen in support of non-classical homogeneous nucleation mechanisms that reduce the required activation energy[11-14]. Specifically, a few related mechanisms were proposed according to which an amorphous dense phase is first formed that then reorders to form a thermodynamically stable crystal nucleus[15-18]. For example, it was shown that for some molecules such as the protein lysozyme a two-step mechanism is responsible for homogeneous crystal nucleation[19]. According to this mechanism the first step is the formation of dense liquid clusters that can be either thermodynamically favorable or short lived thermal fluctuations. The rate determining step is then organization of these dense phases into crystal nuclei. Another non-classical mechanism described in the literature is cluster attachment where small crystal nuclei collide and merge to form a larger, more stable, crystal nucleus[15,20,21]. There have been a few attempts at imaging crystal growth by electron microscopy[22-24] and force microscopy[25,26] in order to elucidate crystallization mechanisms. The observations confirm some of the non-classical crystallization mechanisms. However, we know of no example that has shown formation of crystal nuclei in a real time measurement with molecular detail.

Polyoxometalates are a class of polyanionic compounds typically containing high-valent group 5 and 6 addenda atoms, such as tungsten or molybdenum, bridged by oxygen atoms[27]. They can also be formed with other metals as addenda atoms, including actinides[28]. These molecular clusters form a large class of structures ranging in diameter from roughly 0.4 to 4 nm, often including heteroatoms such as phosphorous or silicon as structural scaffolds[29]. Replacement of one or more oxygen atoms with fluorine forms the subclass of polyfluoroxometalates[30]. The relatively large size of polyoxometalates and their inclusion of many electron rich tungsten addenda atoms have been used in the past for their high contrast in transmission electron microscopy (TEM) and X-ray diffraction measurements, where contrast stems from electron content and low contrast is often an issue[31,32]. Another notable feature is that the solubility of polyoxometalates is counter-cation dependent. For example, in water, the solubility of group 6 polyoxometalates decreases as a function of the atomic weight of alkali metal cation when going from lithium to cesium[33]. This fact can be used for moderating the tendency of a polyoxometalate to aggregate and to precipitate, especially with highly charged polyoxometalates such as the one used by us.

In this research we prepared homogeneous aqueous solutions of an oval polyfluoroxometalate in the presence of NaCl. Direct imaging by cryo transmission electron microscopy (cryo-TEM) of a vitrified solution enables the observation of crystal nucleation driven by electron beam irradiation that causes local heating. From homogeneous solutions, nucleation was observed to take place by a molecular attachment mechanism. Two-dimensional crystals are formed with a lattice structure that correlates quite accurately with the (100) Miller plane of a three-dimensional single crystal structure measured by X-ray diffraction (XRD). Atomistic molecular dynamics (MD) simulations show that the interaction between the oblong polyfluoroxometalate occurs via Na^+-mediated interactions. In the presence of CsCl instead of NaCl amorphous aggregates of the polyfluoroxometalate are pre-

formed in the aqueous solution. A similar cryo-TEM experiment shows that also here crystal nuclei are formed, in a lower energy process.

A 4.5 mM solution of quasi-Wells Dawson polyfluoroxometalate, $K_8[H_2F_6NaMn^{IV}(OH)W_{17}O_{55}]$ (MnPFOM) (Figure S1) and 70 mM NaCl was heated to 60 °C and deposited on a quantifoil TEM grid. The grid was then rapidly cooled to -180 °C in liquid ethane in order for vitrification to occur. In essence, by cooling the solution a highly super-saturated, kinetically stable glass solution was prepared. The vitrified solution was imaged by cryo-TEM at -170 °C. Images were recorded continuously while the sample was irradiated with the TEM electron beam at low dose rate, in order to monitor the motion of MnPFOM in solution as thermal energy is introduced by the electron beam. This added thermal energy shifts the vitrified supersaturated solution towards equilibrium. Figure 1 displays snapshots that were extracted from such a series of images. Single MnPFOM molecules can be easily identified in these images, each represented by a dark spot.

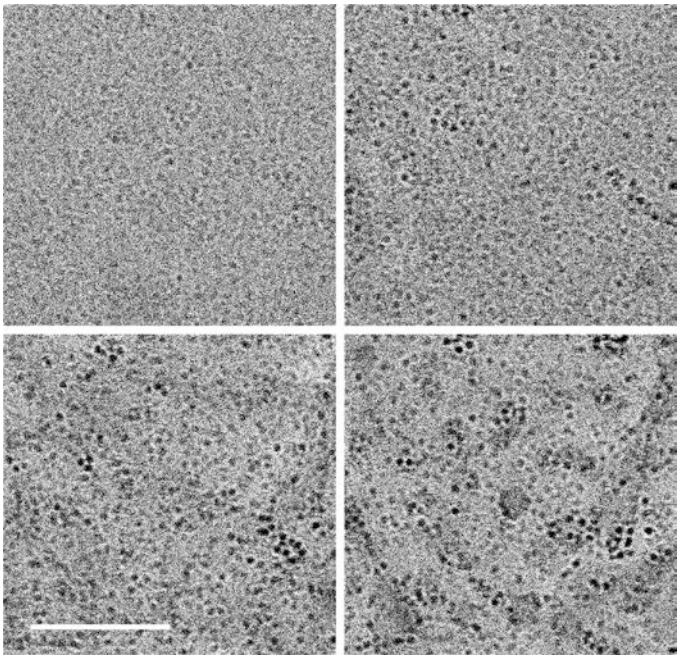

Figure 1. Time series of MnPFOM aggregation with NaCl. Left to right, top to bottom. Aggregation of MnPFOM molecules under illumination with the electron microscope beam in a cryo-TEM experiment. Cumulative electron doses applied are 0, $1.7*10^3$, $3.5*10^3$ and

$5.3*10^3$ e/Å^2 respectively. The scale bar is 50 nm. A dark dot is associated with the cluster of tungsten atoms in a single MnPFOM molecule.

Figure 1, top left, shows that the solution is initially homogenous. Upon accumulation of exposure dose the MnPFOM molecules assemble to form approximately round aggregates in a process of molecular attachment. A subsequent motion within the aggregate leads to the most stable location, Figure 1, Movies S1 and S2. The initially formed round aggregates, consisting of approximately 5-15 molecules, can also interact with each other to form larger aggregates of 15-45 molecules in a process of cluster attachment, Movie S3. Repeating the same procedure without addition of the NaCl salt resulted in no aggregation, Movie S4. It should be mentioned that due to the high accumulated electron dose, some damage to the sample and ice formation was observed in some measurements. This does not, however, significantly affect the observed nucleation of MnPFOM, as the same processes can be seen in all cases also in sample areas where there is no ice formation.

In order to get a three-dimensional picture of the formed clusters, a TEM tomogram of the final product was measured, Movie S5. This tomogram shows that crystal nucleation occurred primarily in the xy-plane of the TEM foil with very little growth along the z-axis. The lack of growth along the z-axis has both physical and chemical explanations. Physically, a vitrified water droplet in a quantifoil grid hole has the dimensions of 1.3 µm on both x- and y-axes, but only about 50-200 nm on the z-axis[34]. During irradiation by the electron beam, vitrified ice sublimes and the drop thickness decreases down to 30 nm as can be seen in the tomogram, Figure S2. This means that there are fewer molecules dispersed within the z axis. It is also possible that some of the growth occurs on the surface of the vitrified solution during sublimation. Chemically, initial crystal growth is expected to occur on the plane that is thermodynamically most saturated. In our case, supersaturation is caused by a large amount of

NaCl that was added to the solution, which acted as a driving force for nucleation. The plane that contains Na^+ counter cations is expected therefore to grow most rapidly as shown below.

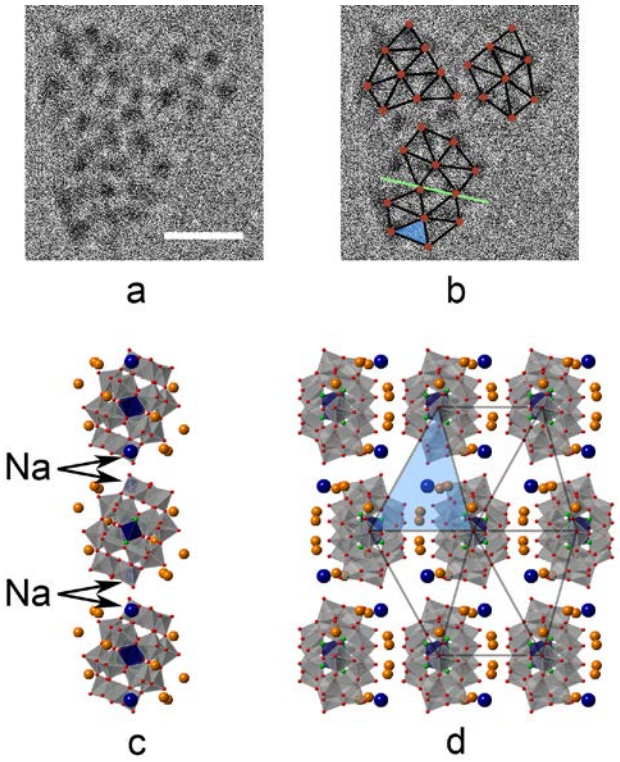

Figure 2. Correlation between cryo-TEM images and the crystal structure. a. TEM image showing three colliding clusters. The scale bar is 10 nm. b. Relative positions of molecules derived from the XRD crystal structure are overlayed (brown) with the TEM image. A twinning plane is shown (green line). c and d. Projections of the (100) plane from XRD crystal structure viewed along the <010> and <100> directions, respectively. Na – blue, K – brown, W – grey, O – red, F – green. Arrows in (2c) refer to Na atoms behind and in front of the MnPFOM molecules. Structural water was omitted and the Na atom size has been increased for clarity.

Figure 2a shows part of a non-tilted image taken from the tomography tilt series. Three colliding clusters of crystal nuclei are seen. Figure 2d presents the molecular crystal packing of MnPFOM facing the (100) Miller plane. The crystallographic data are presented in a cif file in the extended data section and were obtained from an XRD of a single crystal grown from a solution MnPFOM and NaCl at 3 °C. For a discussion of the two dimensional plane

group formed by MnPFOM molecules on the (100) plane of the three dimensional crystal structure, see Figure S3. Overlapping the non-tilted image from the tomography, Figure 2a, and molecular arrangement along the (100) plane of MnPFOM from the crystal structure reveals that although the distances between MnPFOM molecules are longer in the tomography due to trapping of water molecules, the crystalline symmetry is preserved. Indeed there is an excellent fit between the packing symmetry in the crystal nuclei and the eventually formed single crystal, Figure 2b. It should be noted that due to the small number of molecules per nucleus it is not reasonable to expect an exact periodicity since edge effects and random fluctuations play a large role in the ordering of this system. This is also apparent by the twinning observed in the image. However, the approximate crystal lattice found indicates that the crystal nuclei are indeed proto-crystalline.

A further analysis of the crystal structure obtained by XRD reveals, as stated above, that the (100) plane contains Na^+ counter cations, Figure 2c, which are located in the center of every three adjacent MnPFOM molecules, Figure 2d. The Na^+ cations are therefore essential for growth of a crystal nucleus based on the (100) plane. On the other hand the placement of K^+ counter cations is outside the (100) plane and they do not participate in the formation of crystal nuclei. It is clear that most of the water molecules initially present in the interstitial space of the homogeneous solution are removed during the formation of crystal nuclei. There remains only one layer of water molecules, that is 6.2 water molecules per MnPFOM, in the (100) plane to buffer between the highly negatively charged MnPFOM molecules, Figure S4.

In this context it is interesting to note that the sodium counter-cation bridges directly between two MnPFOM molecules, where one is bound by two terminal and one bridging oxygen atoms while the other is bound by a single terminal oxygen atom. The W/Mn disordered site nearest to this sodium counter-cation is the one with most Mn occupancy, where the terminal hydroxyo of this Mn site binds to the sodium ion. This is probably due to the increased basicity of this site relative to all other terminal oxygens.

In order to further understand the observed nucleation process at an atomistic level, we performed molecular dynamics (MD) simulations of polyoxometalates in supersaturated salt solutions at the concentrations used for the formation of proto-crystals. From the 10 ns MD trajectories it was possible to observe aggregation between MnPFOM anions, a phenomena viewed as the initial stage for processes such ion condensation and crystal nucleation[35]. A box of dimensions 25.1× 24.9 × 25.2 nm^3 was filled in with 20 MnPFOM anions, 160 K^+ counter-ions, 330 molecules of NaCl, and 17887 water molecules. The computational details section provides a detailed description of the MD simulations and the movies in the Extended Data display representative simulation periods ranging from ~0.5 to ~1.1 ns. The MnPFOM molecules in the simulation aggregated into dimers and trimers via cation-mediated interactions as shown in Figure 3 and S5, and Movie S6.

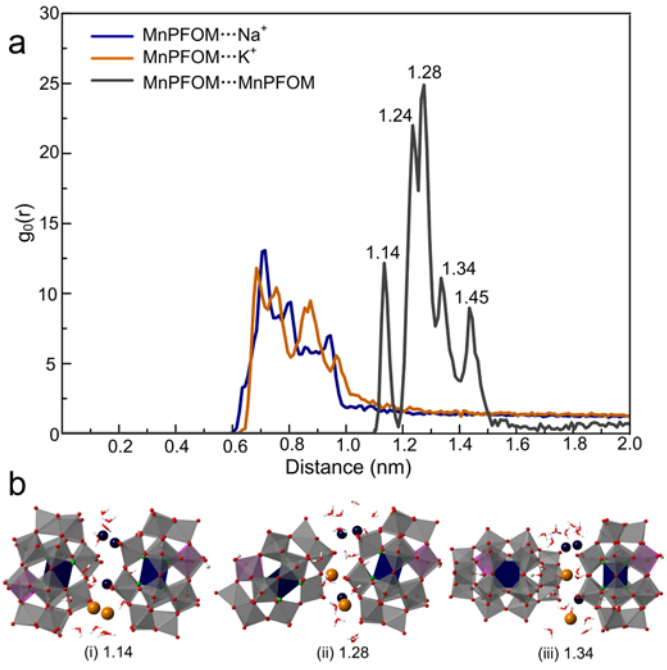

Figure 3. Molecular dynamics calculations for the system with NaCl. a. Radial distribution functions between MnPFOM···Na^+ (dark blue), MnPFOM···K^+ (brown) and MnPFOM···MnPFOM (dark grey). The internal Na atom of the MnPFOM structure was used as reference for MnPFOM···MnPFOM RDF. b. Representative snapshots for MnPFOM··· MnPFOM dimers corresponding to different RDF peaks. Additional modes appear in Figure

S5. (i) Interaction along their long axis at 1.14 nm, (ii) diagonal interaction at 1.28 nm and (iii) perpendicular interaction between short and long axis at 1.34 nm. The tilt angle between the long axes are 8, 48 and 93º for (i) - (iii), respectively.

The radial distribution function (RDF) between MnPFOM anions exhibits several peaks in range from 1.1 to 1.5 nm, Figure 3a. The first peak centered at 1.14 nm is separated from the others and corresponds to a well-defined binding mode with the closest MnPFOM···MnPFOM contact. In this interaction oblong MnPFOM molecules dimerize along their long axis with Na^+ cations playing the role of a bridge connecting the two MnPFOMs, see Figure 3b (i) for a representative snapshot. It is notable that the experiment shows that indeed in the crystal nuclei and single crystal, the closest contact between the MnPFOM molecules are those aligned along the long axes indicating that this aggregate could initiate the monomer-by-monomer addition to build the crystal. As Figure 3b shows, the other peaks correspond to interactions where a MnPFOM molecule interacts diagonally (ii) or from short axis to the long axis of a second molecule (iii). Here Na^+ and K^+ cations also link the MnPFOM anions, indicating that cation-induced effect overcomes the Coulomb repulsive interaction between two anions. It should be noted that in the absence of NaCl there was neither nucleation in cryo-TEM experiments nor formation of aggregates in the molecular dynamics simulations (see Figure S6 and Movie S7), further supporting that the NaCl salt acts as a driving force for nucleation.

It has been suggested that in some cases crystal nucleation begins with the formation of non-periodic amorphous aggregates that subsequently reorganize to form crystalline material[15,19]. We, when substituting NaCl with CsCl, now observe this mechanism for crystal formation. We had previously shown by cryo-TEM that solutions of MnPFOM with CsCl form colloids of two types – large spherical colloids and long chain dendritic type structures[34]. Irradiating the dendritic structures with the electron beam results in a collapse of

the structure into crystal nuclei that are both larger than previously described for NaCl and non-symmetrical, conforming to the directionality of the dendritic structure that existed beforehand, Figure 4, Movies S8 and S9. Proto-crystallinity of these samples can be shown by observation of crystal facets similarly to what was shown when MnPFOM nucleated in the NaCl sample, Figure S7. However, rapid changes in this sample during electron beam irradiation did not allow for tomographic measurements and therefore the three dimensional structure could not be observed.

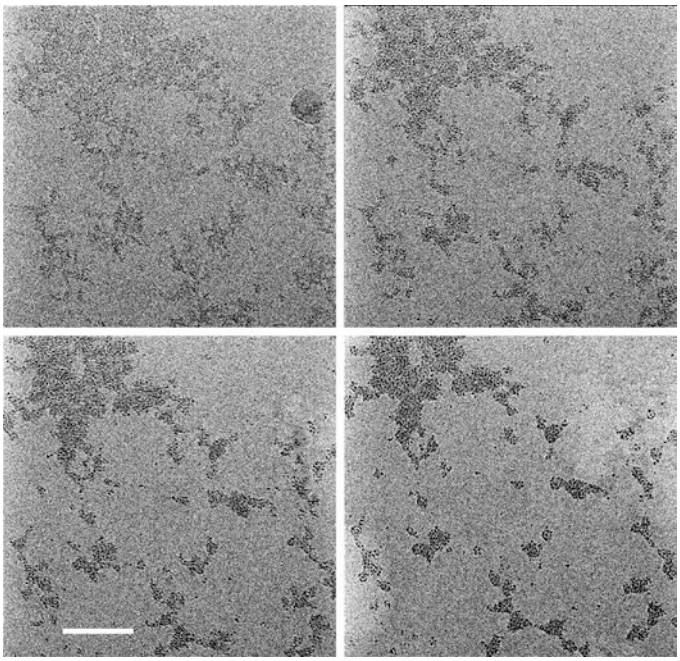

Figure 4. Time series of MnPFOM aggregation with CsCl. Left to right, top to bottom. Aggregation of MnPFOM molecules in the presence of CsCl under the electron microscope beam. Accumulative electron doses applied are 0, $0.37*10^3$, $0.74*10^3$ and $1.2*10^3$ e/Å^2 respectively. The scale bar is 50nm. Dark dots are associated with tungsten containing MnPFOM molecules.

It is apparent that a lower activation barrier exists for crystallization of a non-ordered aggregate of MnPFOM in the presence of CsCl than for crystallization via molecular attachment from a homogeneous solution of MnPFOM in the presence of NaCl. Nucleation from the homogeneous solution required about $5*10^3$ e/Å^2 for full crystal nuclei formation,

Movie S1, while from a non-ordered aggregate only about $1.2*10^3$ e/Å^2 were necessary, Movie S8. Moreover, the smaller amount of energy used for nucleation of MnPFOM led to a migration of MnPFOM molecules over longer distances within the vitrified solution and therefore also formed larger crystal nuclei. The change in mechanism between the two vitrified solutions is directly related to a large change in solubility and attraction between a MnPFOM polyanion and the added cation, Na^+ or Cs^+. Therefore, addition of Cs^+ cations to the solution causes some aggregation and long-distance interactions even in non-saturated solutions, without causing formation of precipitate[36]. On the other hand, Na^+ cations that have only a limited attraction to MnPFOM polyanions cause only local interactions and allow the addition of molecules one by one, with enough time to reorganize to the most stable, ordered, state between molecular addition events.

Summarizing, solutions of MnPFOM and MCl (M = Na or Cs) were vitrified and imaged by cryo-TEM. Since at cryo-TEM temperatures both solutions are super-saturated, addition of thermal energy by electron-beam irradiation induced formation of two-dimensional crystal nuclei that were followed in molecular detail by cryo-TEM imaging and have a lattice structure that correlates well with the (100) plane of a single crystal. Although in both cases the small nuclei formed were found to be proto-crystalline, with a semi-periodic lattice structure, a large difference was found in the nucleation mechanism. While Na^+ cations induced a classical molecular attachment mechanism together with some cluster attachment, Cs^+ cations induced a dense phase crystallization mechanism where MnPFOM molecules first form a non-ordered aggregate that later collapses into an ordered lattice. The molecular attachment mechanism was experimentally found to have a significantly higher activation energy than the collapse of a non-ordered aggregate in the dense phase mechanism as has been also shown by computer simulations[37]. It should be noted that the largely two dimensional structure formed raises the possibility of different crystallization mechanisms being responsible for growth of different crystal facets. Although the growth of an

enthalpically driven two-dimensional crystal structure was observed, it is possible that the less saturated <100> direction that did not grow by molecular attachment will over time eventually grow by cluster attachment. Such an attachment will release a large amount of K^+ counter cations and water molecules back to solution, therefore increasing the entropy of the crystallization process.

Methods

Synthesis - The synthesis of $K_8[H_2F_6NaMn^{IV}(OH)W_{17}O_{55}]\cdot 15H_2O$ was done according to a previously reported procedure[36]. First the Zn(II) substituted PFOM was prepared by dissolving 44 g of $Na_2WO_4\cdot 2H_2O$ in 100 mL of de-ionized water and heating to 80-85 °C. To this solution were added 14 mL of 40% HF bringing it to pH = 4.5. The solution was then stirred for 1 hour and filtered. The filtrate was reheated to 80 °C and a solution of 7 g $Zn(CH_3CO_2)_2\cdot 2H_2O$ in 10 mL de-ionized water was added dropwise. The solution was let stir for an additional 1 hour and filtered. Note that carefully controlling the temperature ensures that the zinc atom is substituted at the belt position only. This filtrate was precipitated by addition of 4.5 g KCl and the precipitate was recrystallized in 5.5 mL de-ionized water. Yield – 3 g. Then 3 g Zn(II)PFOM dissolved in 27 mL acetate buffer, pH=5, were heated to 50 °C and 324 mg $MnSO_4\cdot H2O$ in 2 mL acetate buffer, pH=5, were added dropwise. The solution turned brown, was stirred for 30 min and then cooled. Mn(II)PFOM was precipitated with a saturated solution of KCl. Yield - 2.4 g (80%). 2g of Mn(II)PFOM were dissolved in 35 mL de-ionized water; 2g of Oxone were added and the solution was heated to 80°C. The solution changed color from light brown to purple and finally to dark brown, where upon it was cooled in ice water and Mn(IV)PFOM was collected by precipitation with saturated KCl. Yield – 1.2 g (60%).

Electron Microscopy (**TEM)** - Samples for electron microscopy were prepared from solutions of 4.5 mM Mn(IV)-OH-PFOM and 70 mM of MCl (M=Na, or Cs) at 60 °C. A drop

of solution was put on a Quantifoil grid (R1.2/1.3 300 mesh copper from EMS) kept at high humidity and maintained at 60 °C in the chamber of the automated plunging apparatus (Leica EM-GP). The grid was then blotted with filter paper and plunged into liquid ethane. Samples were transferred under liquid nitrogen to a Gatan 626 cryoholder, and visualized by TEM under low-dose cryo-conditions with a Tecnai G2 TWIN-F20 microscope. An adequate amount of phase contrast of MnPFOM molecules was obtained at an underdefocus of approx. 500 nm. The corresponding disk of confusion due to focus blur[38] is about 1.2 nm for a MnPFOM molecule. TEM time series images were recorded on a Gatan K2 Summit electron direct detection camera (Gatan Inc., Pleasanton, CA) operated in counting mode or a Gatan US4000 CCD camera (Movies S2 and S9). Na crystallization sample was irradiated with 45 e/Å/s at 200 keV. Cs sample was irradiated with 19 e/Å/s at 200 keV. Tomography images were recorded on a Gatan K2 Summit electron direct detection camera operated in counting mode.

X-ray Crystallography - An aqueous solution of 27 mM Mn(IV)PFOM and 420 mM NaCl was crystalized at 3 °C. The formed crystals were heat sensitive and therefore were kept in liquid N_2 until their measurement. **Crystal data**: $F_6K_6Na_3Mn_1W_{17}O_{76}$ ($F_6K_6Na_1Mn_1W_{17}O_{56}$+2*Na+20*O) yellow, 0.05 x 0.12 x 0.18 mm^3, Monoclinic, C2/c, a=22.586(5)Å, b=12.292(3)Å, c=29.421(6)Å, β=92.34(3)° from 20 degrees of data, T=100(2)K, V=81.61(3) $Å^3$, Z=4, Fw=4813.96, Dc=3.918 $Mg.m^{-3}$, μ=24.439 mm^{-1}. **Data collection and processing**: Bruker Apex2 KappaCCD diffractometer, MoKα (λ=0.71073Å), graphite monochromator, 19886 reflections collected, -26≤h≤27, -7≤k≤14, -35≤l≤35, frame scan width = 0.5°, scan speed 1° per 360 sec, typical peak mosaicity 0.82°, 7399 independent reflections (R-int =0.0740). The data were processed with Bruker Apex2 software. **Solution and refinement**: Structure solved with SHELXT. Full matrix least-squares refinement based on F^2 with SHELXL-2014/7. 550 parameters with 85 restraints, final R_1= 0.0495 (based on

F^2) for data with I>2σ(I) and, R_1= 0.0854 on 7399 reflections, goodness-of-fit on F^2 = 1.018, largest electron density peak = 2.506 $Å^{-3}$, deepest hole= -1.873 $Å^{-3}$.

Computational Details - Classical MD simulations were performed for **two** different systems, and the detailed composition of the systems was listed in Table S1.The systems were simulated by classical MD using GROMACS 4.5.4 software[39] and the AMBER99 force field[40], which has been successfully employed to study the aggregation behaviour of polyoxometalate anions in solution by Chaumont and Wipff[41]. The potential energy *U* is empirically described by a sum of bond (k_b and b_0 parameters), angle (k_θ and θ_0 parameters), and dihedral deformation energies (V_n parameter) and pair-wise additive 1-6-12 (electrostatic, q_i, and van der Waals, R^*_{ij} and ε_{ij} parameters) interaction between non bonded atoms, see eq. 1:

$$U = \sum_{bonds} k_b(b - b_0)^2 + \sum_{angles} k_\theta(\theta - \theta_0)^2 + + \sum_{dihedrals} \sum_{n} V_n\left(1 + cos(n\varphi - \gamma)\right) + + \sum_{i<j} \left[\frac{q_i q_j}{R_{ij}} - 2\varepsilon_{ij}\left(\frac{R^*_{ij}}{R_{ij}}\right)^6 + \varepsilon_{ij}\left(\frac{R^*_{ij}}{R_{ij}}\right)^{12}\right] \quad (1)$$

The parameters for the MnPFOM anion, $[H_2F_6NaMn^{IV}(OH)W_{17}O_{55}]^{8-}$, were obtained following the procedure of Bonet-Avalos, Bo, Poblet *et* al[42]. We used CHELPG atomic charges derived from electrostatic potential. They were obtained with the Gaussian09 package at the DFT level (BP86 functional) using the LANL2DZ basis set. The geometry of MnPFOM anion was previously obtained by optimization at BP86/TZ2P level with the ADF2012 package[43]. The core potentials for the atoms were generated with the DIRAC program by using the scalar relativistic approach ZORA[44]. In order to consider the solvent effect, the water was included in the calculations by using the conductor-like screening model (COSMO)[45] with ionic radii of 1.40 (O),

2.10 (W), 1.84 (Na), 1.39 (F), 1.08 (H), and 1.97 (Mn) Å. Both the doublet and quartet spin states of Mn(IV) were calculated, the results showing that the quartet is 18.5 kcal mol^{-1} more stable than the doublet. Only the ground-state structure was considered for setting the parameters of molecular dynamics simulations. The set of Lennard-Jones parameters for W and O atoms were taken from previous work[42], for Mn we used those defined for Fe in AMBER99 force field, and for F we used those proposed by Dang[46]. We should mention that the W, Mn, F and Na atoms of MnPFOM structure are embedded within a shell of oxygen atoms, and consequently, their definition in the force field have a minor effect on the intermolecular interactions of MnPFOM with the solvent, the cations, and the other anions.

For the MD simulations 20 MnPFOM anions and the corresponding K^+ counter cations were embedded in a water solvent box of 25.1 × 24.9 × 25.2 nm^3. Then we added 330 NaCl molecules (**1**) or no additional salt (**2**), see Table S1. Water was represented with the TIP3P model[47]. All simulations were performed with 3D-periodic boundary conditions using an atom cutoff of 14 Å for 1-4 van der Waals and of 9 Å for 1-4 Coulombic interactions and corrected for long-range electrostatics by using the particle-particle mesh Ewald (PME) summation method[48]. The simulations were performed at 300 K starting with random velocities. The temperature was controlled by coupling the system to a thermal bath[49] with a relaxation time of 0.5 ps to keep the NVT microcanonical conditions. In the NPT simulations, the pressure was similarly coupled to a barostat with a relaxation time of 0.2 ps. Newton equations of motion were integrated using the leap-frog algorithm[50], and a time step of 1 fs. Before the 10 ns production runs, the systems were equilibrated as follows; (i) 10000 steps of energy minimization; (ii) 250 ps of simulation at constant volume (NVT), in which the MnPFOM structures were kept fixed; (ii) 250 ps of NVT simulation; and (iv) 250 ps of

simulation at constant pressure of 1 atm (NPT) to equilibrate the solution density and rescale the simulation box.

References and Notes

1. Gibbs, J. W., On the equilibrium of heterogeneous substances. *Trans. Connect. Acad. Sci.* **3**, 108-248 (1876).

2. Gibbs, J. W., On the equilibrium of heterogeneous substances. *Trans. Connect. Acad. Sci.* **16**, 343-524 (1878).

3. Schuth, F., Bussian, F., Agren, F., Schunk, S. & Linden, M., Techniques for analyzing the early stages of crystallization reactions. *Solid State Sciences* **3**, 801-808 (2001).

4. Erdemir, D., Lee, A. Y. & Myerson, A. S., Nucleation of crystals from solution: Classical and two-step models. *Acc. Chem. Res.* **42**, 621-629 (2009).

5. Chayen, N. E., Saridakis, E. & Sear, R. P., Experiment and theory for heterogeneous nucleation of protein crystals in a porous medium. *Proc. Natl. Acad. Sci.* **103**, 597-601 (2006).

6. Varanasi, K. K., Hsu, M., Bhate, N., Yang, W. & Deng, T., Spatial control in the heterogeneous nucleation of water. *Appl. Phys. Lett.* **95**, 094101 (2009).

7. Kashchiev, D. & van Rosmalen, G. M., Review: Nucleation in solutions revisited. *Cryst. Res. Technol.* **38**, 555-574 (2003).

8. Watson, J. N., Iton, L. E., Keir, R. I., Thomas, J. C., Dowling, T. L. & White, J. W., TPA−Silicalite crystallization from homogeneous solution: Kinetics and mechanism of nucleation and growth. *J. Phys. Chem. B* **101**, 10094–10104 (1997).

9. Vekilov, P. G. & Galkin, O., Are nucleation kinetics of protein crystals similar to those of liquid droplets? *J. Am. Chem. Soc.* **122**, 156-163 (2000).

10. Galkin, O. & Vekilov, P. G., Direct determination of the nucleation rates of protein crystals. *J. Phys. Chem. B* **103**, 10965–10971 (1999).

11. Banfield, J. F., Welch, S. A., Zhang, H., Ebert, T. T. & Penn, R. L., Aggregation-based crystal growth and microstructure development in natural iron oxyhydroxide biomineralization products. *Science* **289**, 751-754 (2000).

12. Baumgartner, J., Dey, A., Bomans, P. H. H., Le Coadou, C., Frantzl, P., Sommerdijk, N. A. J. M. & Faivre, D., Nucleation and growth of magnetite from solution. *Nat. Mater.* **12**, 310-314 (2013).

13. Van Driessche, A. E. S., Benning, L. G., Rodriguez-Blanco, J. D., Ossorio, M., Bots, P. & García-Ruiz, J. M., The Role and implications of bassanite as a stable precursor phase to gypsum precipitation. *Science* **336**, 69-72 (2012).

14. Gebauer, D., Volkel, A. & Colfen, H., Stable prenucleation calcium carbonate clusters. *Science* **322**, 1819-1822 (2008).

15. De Yoreo, J. J., Gilbert, P. U. P. A., Sommerdijk, N. A. J. M., Penn, R. L., Whitelam, S., Joester, D., Zhang, H., Rimer, J. D., Navrotsky, A., Banfield, J. F., Wallace, A. F., Michel, F. F., Meldrum, F. C., Cölfen, H. & Dove, P. M., Crystallization by particle attachment in synthetic, biogenic, and geologic environments. *Science* **349**, 6760-1 -6760-6 (2015).

16. ten Wolde, P. R. & Frenkel, D., Enhancement of protein crystal nucleation by critical density fluctuations. *Science* **277**, 1975-1978 (1997).

17. Wolf, S. E., Leiterer, J., Kappl, M., Emmerling, F. & Tremel, W., Early Homogenous amorphous precursor stages of calcium carbonate and subsequent crystal growth in levitated droplets. *J. Am. Chem. Soc.* **130**, 12342-12347 (2008).

18. Galkin, O., Chen, K., Nagel, R. L., Hirsch, R. E. & Vekilov, P. G., Liquid–liquid separation in solutions of normal and sickle cell hemoglobin. *Proc. Natl. Acad. Sci.* **99**, 8479-8483 (2002).

19. Vekilov, P. G., Nucleation. *Cryst. Growth Design* **10**, 5007-5019 (2010).

20. Yuwono, V. M., Burrows, N. D., Soltis, J. A. & Penn, R. L., Oriented aggregation: Formation and transformation of mesocrystal intermediates revealed. *J. Am. Chem. Soc.* **132**, 2163-2165 (2010).

21. Niederberger, M. & Colfen, H., Oriented attachment and mesocrystals: Non-classical crystallization mechanisms based on nanoparticle assembly. *Phys. Chem. Chem. Phys.* **8**, 3271-3287 (2006).

22. Nielsen, M. H., Aloni, S. & De Yoreo, J. J., In situ TEM imaging of CaCO3 nucleation reveals coexistence of direct and indirect pathways. *Science* **345**, 1158-1162 (2014).

23. Li, D., Nielsen, M. H., Lee, J. R. I., Frandsen, C., Banfield, J. F. & De Yoreo, J. J., Direction-specific interactions control crystal growth by oriented attachment. *Science* **336**, 1014-1018 (2012).

24. Chen, Q., Cho, H., Manthiram, K., Yoshida, M., Ye, X. & Alivisatos, A. P., Interaction potentials of anisotropic nanocrystals from the trajectory sampling of particle motion using in situ liquid phase transmission electron microscopy. *ACS Cent. Sci.* **1**, 33-39 (2015).

25. Lupulescu, A. I. & Rimer, J. D., In situ imaging of silicalite-1 surface growth reveals the mechanism of crystallization. *Science* **344**, 729-732 (2014).

26. Yau, S. T. & Vekilov, P. G., Direct observation of nucleus structure and nucleation pathways in Apoferritin crystallization. *J. Am. Chem. Soc.* **123**, 1080-1089 (2001).

27. Pope, M. T., *Heteropoly and Isopoly Oxometalates* (Springer, 1983).

28. Qiu, J. & Burns, P. C., Clusters of actinides with oxide, peroxide or hydroxide bridges. *Chem. Rev.* **113**, 1097-1120 (2013).

29. Liu, T., Diemann, E., Li, H., Dress, A. W. M. & Muller, A., Self-assembly in aqueous solution of wheel-shaped Mo154 oxide clusters into vesicles. *Nature* **426**, 59-62 (2003).

30. Chauveau, F., Doppelt, P. & Lefebvre, J., Fluorotungstates of the metatungstate family: identification and properties of one compound of the 2-18 series. *Inorg. Chem.* **19**, 2803-2806 (1980).

31. Sharet, S., Sandars, E., Wang, Y., Zeiri, O., Neyman, A., Meshi, L. & Weinstock, I. A., Orientations of polyoxometalate anions on gold nanoparticles. *Dalton Trans.* **41**, 9849-9851 (2012).

32. Soltis, J. A., Wallace, C. M., Penn, R. L. & Burns, P. C., Cation-Dependent Hierarchical Assembly of U60 Nanoclusters into Macro-Ion Assemblies Imaged via Cryogenic Transmission Electron Microscopy. *J. Am. Chem. Soc.* **138**, 191-198 (2016).

33. Spitsyn, V. I. & Babaev, N. B., Solubility of difficultly soluble alkali metal heteropolyacids. *Russ. J. Inorg. Chem.* **5**, 580-585 (1960).

34. Cho, H. J., Hyun, J. K., Kim, J. G., Jeong, H. S., Park, H. N., You, D. J. & Jung, H. S., Measurement of ice thickness on vitreous ice embedded cryo-EM grids: investigation of optimizing condition for visualizing macromolecules. *J. Anal. Sci. Technol.* **4**, 7 (2013).

35. Rao, P. R. V. & Kolarik, Z., A review of third phase formation in extraction of actinides by neutral organophosphorus extractants. *Solvent Extr. Ion Exch.* **14**, 955–993 (1996).

36. Schreiber, R. E., Cohen, H., Leitus, G., Wolf, S. G., Zhou, A., Que Jr., L. & Neumann, R., Reactivity and O2 formation by Mn(IV)- and Mn(V)-hydroxo species stabilized within a polyfluoroxometalate framework. *J. Am. Chem. Soc.* **137**, 8738-8748 (2015).

37. Wallace, A. F., Hedges, L. O., Fernendez-Martinez, A., Raiteri, P., Gale, J. D., Waychunas, G. A., Whitelam, S., Banfield, J. F. & De Yoreo, J. J., Microscopic evidence for liquid-liquid separation in supersaturated CaCO3 solutions. *Science* **341**, 885-889 (2012).

38. Egerton R., *Physical Principles of Electron Microscopy: An Introduction to TEM, SEM, and AEM, 1st edition* Ch. 3 (Springer 2005).

39. Pronk, S., Páll, S., Schulz, R., Larsson, P., Bjelkmar, P., Apostolov, R., Shirts, M. R., Smith, J. C., Kasson, P. M., Spoel, D., van der Hess, B. & Lindahl, E. , GROMACS 4.5: a high-throughput and highly parallel open source molecular simulation toolkit. *Bioinformatics*, 1-10 (2013).

40. Wang, J. M., Cieplak, P. & Kollman, P. A., How well does a restrained electrostatic potential (RESP) model perform in calculating conformational energies of organic and biological molecules? *J. Comput. Chem.*, **21**, 1049-1074 (2000).

41. Chaumont, A. & Wipff, G., Ion aggregation in concentrated aqueous and methanol solutions of polyoxometallates Keggin anions: the effect of counterions investigated by molecular dynamics simulations. *Phys. Chem. Chem. Phys*., **10**, 6940-6953(2008).

42. López, X., Nieto-Draghi, C., Bo, C., Bonet-Avalos, J. & Poblet, J. M., Polyoxometalates in solution: Molecular dynamics simulations on the alpha-$PW_12O_{40}^{3-}$ Keggin anion in aqueous media. *J. Phys. Chem. A*, **109**, 1216-1222 (2005).

43. Hay, P. J., Wadt & W. R., *Ab initio* effective core potentials for molecular calculations. Potentials for the transition metal atoms Sc to Hg. *J. Chem. Phys*., **82**, 270-283(1985).

44. Lenthe, E. V., Ehlers, A. & Baerends, E. J., Geometry optimizations in the zero order regular approximation for relativistic effects. *J. Chem. Phys*., **110**, 8943–8953(1999).

45. Pye, C. C. & Ziegler, T., An implementation of the conductor-like screening model of solvation within the Amsterdam density functional package. *Theor. Chem. Acc*. **101,** 396-408 (1999)

46. Dang, L X., Development of Nonadditive Intermolecular Potentials Using Molecular-Dynamics - Solvation of Li^+ and F^- Ions in Polarizable Water. *J.Chem. Phys.*, **96**, 6970-6977 (1992).

47. Jorgensen, W. L., Chandrasekhar, J., Madura, J. D. , Impey, R. W. & Klein, M. L. , Comparison of simple potential functions for simulating liquid water. *J. Chem. Phys*. **79**, 926 (1983).

48. Darden, T., York, D. & Pedersen, L., Particle mesh Ewald: An N·log(N) method for Ewald sums in large systems. *J. Chem. Phys*., **98**, 10089-10092 (1993).

49. Bussi, G., Donadio, D. & Parrinello, M., Canonical sampling through velocity rescaling. *J. Chem. Phys.*, **126**, 014101 (2007).

50. Hockney, R. W., Goel, S. P., Eastwood, J. W., Quiet high-resolution computer models of a plasma. *J. Comp. Phys.* **14**, 148–158 (1974).

Supplementary Information is linked to the online version of the paper at www.nature.com/nature

Acknowledgments:

The research at the Weizmann Institute of Science was funded by the Israel Science Foundation grant #763/14 and electron microscopy experiments were partially funded by Irving and Cherna Moscowitz Center for Nano and Bio-Nano Imaging of the Weizmann Institute of Science. R.N. is the Rebecca and Israel Sieff Professor of Chemistry. Research at Universitat Rovira i Virgili was supported by the Spanish Ministry of Science and Innovation (grant CTQ2014-52774-P) and the Generalitat de Catalunya (2014SGR199 and XRQTC). J.M.P. thanks ICREA foundation for an ICREA ACADEMIA award.

Author Contributions:

RES carried out the majority of the research, RES, LH and SGW carried out electron microscopy measurements and analyzed tomography data, GL carried out the X-ray diffraction measurements, Z-LL, JJC and JMP did the molecular dynamics calculations and RN supervised the research.

The crystal structure was deposited at the Cambridge Crystallographic Data Center – CDCC 1471002

*Correspondence and requests for materials should be addressed to ronny.neumann@weizmann.ac.il